



Integration of Co-Flow Jet Airfoil with Quasi-Micro-Compressor for High Efficiency Cruise at Different Mach Numbers

Paula A. Barrios * Yan Ren † Kewei Xu ‡ GeCheng Zha §
Dept. of Mechanical and Aerospace Engineering
University of Miami, Coral Gables, Florida 33124
E-mail: gzha@miami.edu

December 2, 2021

Abstract

This paper simulates the integration of a 3D Co-Flow Jet (CFJ) airfoil with a quasi-micro-compressor represented by compressor boundary conditions to study the cruise performance with a variation of Mach numbers. The purpose is to understand how the micro-compressor will operate at different Mach numbers in order to design the CFJ airfoil system with high cruise efficiency. The Mach numbers studied are 0.17, 0.25, and 0.46 to represent a range of cruise conditions for electric airplanes. The airfoil is designed for optimum cruise efficiency, meeting the mission requirements from given geometric dimensions. The micro-compressor is designed to satisfy required total pressure ratio and the dimension of the airfoil with a maximized mass flow rate. At Mach numbers 0.17 and 0.25, micro-compressor design G8A has a low design total pressure ratio of 1.04, while Mach number 0.46 requires a micro-compressor design G5 with a higher design total pressure ratio of 1.17 to compensate for the larger boundary layer loss of the airfoil. CFJ injection and suction ducts are designed with minimum total pressure loss to achieve the high efficiency operating region in the compressor map. The ducts connecting the micro-compressors with the CFJ airfoil have a circular shape at the interface of the micro-compressor and transition to rectangle slots at the airfoil. Design iteration of the ducts is an important step in the integration of CFJ airfoil and micro-compressor by matching the mass flow rate and compressor total pressure ratio to the high efficiency operating line. The micro-compressor outlet is simulated with a swirl profile provided by each of the two compressor designs. The micro-compressor design is only conducted once and is not in the iteration process to save the design cycle. The micro-compressor is thus a quasi-micro-compressor. The simulation of each Mach number is for cruise condition at low angle of attack 5° with a range of 0° to 15° . The results show that by integrating the designs of micro-compressor and CFJ airfoil through duct design, a high efficiency operating line can be achieved with efficiency of about 76% to 82% for Mach number 0.17, 79% to 85% for Mach number 0.25, and 73% to 78% for Mach number 0.46. The study demonstrates that CFJ airfoil design integration with the micro-compressor allows the CFJ aircraft to cruise at a high efficiency operating range of the compressor for a range of Mach numbers.

Nomenclature

<i>CFJ</i>	Co-flow jet
<i>AoA</i>	Angle of attack
<i>LE</i>	Leading edge

* Ph.D. Student

† PostDoc Researcher. Ph.D., AIAA member

‡ PostDoc Researcher. Ph.D.

§ Professor, ASME Fellow, AIAA associate Fellow

TE	Trailing edge
S	Planform area
c	Airfoil chord
U	Flow velocity
q	Dynamic pressure $0.5 \rho U^2$
p	Static pressure
η	Pump efficiency
ρ	Air density
\dot{m}	Mass flow rate
M	Mach number
ω	Pitching moment
P	Pumping power
SD	Suction duct
ID	Injection duct
∞	Free stream conditions
j	Jet conditions
C_L	Lift coefficient $L/(q_\infty S)$
C_D	Drag coefficient $D/(q_\infty S)$
C_M	Moment coefficient
C_μ	Jet momentum coefficient $\dot{m}_j U_j / (q_\infty S)$
$(C_L/C_D)_c$	CFJ airfoil corrected aerodynamic efficiency $L/(D + P/V_\infty)$
$(C_L^2/C_D)_c$	CFJ airfoil productivity efficiency $C_L^2/(C_D + P/V_\infty)$
P_C	Power coefficient $L/(q_\infty S V_\infty)$
P_{tr}	Total pressure ratio between injection and suction
M_∞	Free stream Mach number
P_{inj}	Total injection pressure
P_{suc}	Total suction pressure
V_{inj}/V_∞	Normalized injection velocity

1 Introduction

Minimizing energy consumption centers on high cruise efficiency, especially in creating electric aircraft where it is important to extend range and payload with a limited battery energy density. Active flow control (AFC) is a promising method to enhance aerodynamic performance. However, increasing aircraft aerodynamic efficiency at cruise condition is challenging because the flow is typically benign at low angles of attack. Enhancing cruise efficiency requires AFC to have low energy expenditure with high conversion efficiency. Most efforts to improve cruise efficiency have been made by passive flow controls, including winglet, wing body combination, flying wing configurations, boundary layer ingestion, distributed propulsion, etc. Not much progress has been made to improve subsonic airfoil cruise performance efficiency through AFC.

AFC transfers external energy to the controlled flow to improve the performance of the flow system. For all AFC systems, there are three measures of merit (MoM): 1) effectiveness, 2) power required (PR), and 3) power conversion efficiency (PCE). Effectiveness quantifies performance enhancement, e.g., removal of flow separation, drag reduction, lift increase, stall prevention, noise mitigation, etc. Power required quantifies the AFC power needed to achieve the targeted effectiveness. Power conversion efficiency quantifies the efficiency to convert the external energy (e.g., mechanical, electric, chemical) to energy required by the controlled flow. It determines how much total power will be consumed by the actual flow control system. For AFC to benefit industry realistic

applications, all three MoM matter. The ultimate criterion for an AFC is that the system efficiency gain should be greater than the AFC energy expenditure. Xu et al [1] analyze the CFJ energy expenditure and describe the efficient techniques to implement CFJ.

The Co-Flow Jet (CFJ) airfoil, shown in Fig. 1 is a zero-net mass-flux (ZNMF) AFC method developed by Zha et al. [2, 3, 4, 5, 6, 7, 8, 9, 10, 11, 12, 13, 14, 15, 16, 17, 18, 19] that can dramatically increase the lift coefficient, stall angle of attack, and drag reduction. For the CFJ AFC, a small amount of mass flow is withdrawn into the suction duct located near the TE, pressurized and energized by the micro-compressor, and injected near the LE tangentially to the main flow through the injection slot. The low energy expenditure required by the CFJ enables it to improve cruise productivity efficiency, $C_L^2 / (C_D + P_{C,CFJ})$, substantially compared with conventional design ($P_{C,CFJ}$ is the required power coefficient for CFJ). In other words, CFJ is proven to have high effectiveness and low power required. The actual power consumed by the micro-compressor is $P_{act} = P_{C,CFJ} / \eta$, where η is the CFJ system power conversion efficiency determined by the design of the micro-compressor actuator and the ducts transporting the injection and suction flow. The micro-compressors are able to reach excellent efficiency of over 80% [14, 20, 21]. However, to take advantage of the high efficiency micro-compressors, it is crucial to design the CFJ ducts with minimal loss as an integrated system. This paper focuses on improving the actual power conversion efficiency by optimizing the ducts design and integration with the CFJ airfoil as illustrated in Fig. 2. The goal is to make the CFJ airfoil at cruise operate at a high efficiency region of the compressor map for each Mach number.

The CFJ AFC relies on the micro-compressor actuators to convert the mechanical power to the power required. To achieve high power conversion efficiency, it is important that the CFJ airfoil operating conditions match the micro-compressor operating line with high efficiency. This requires the design of the CFJ airfoil to be integrated with the micro-compressors as shown in Fig. 2, a conclusion reached by Zha et al. [22] and Xu et al. [23]. The purpose of this paper is to numerically design and simulate an integrated CFJ airfoil with the micro-compressor represented by the boundary conditions extracted from the compressors in order to achieve high system energy conversion efficiency at different Mach numbers, 0.17, 0.25, and 0.46.

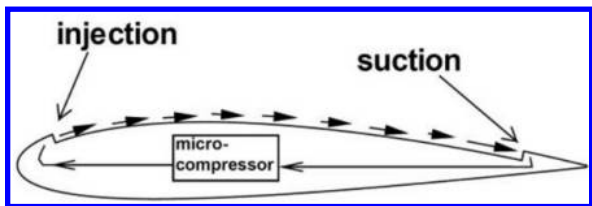


Figure 1: 2D sketch of CFJ airfoil showing the flow direction

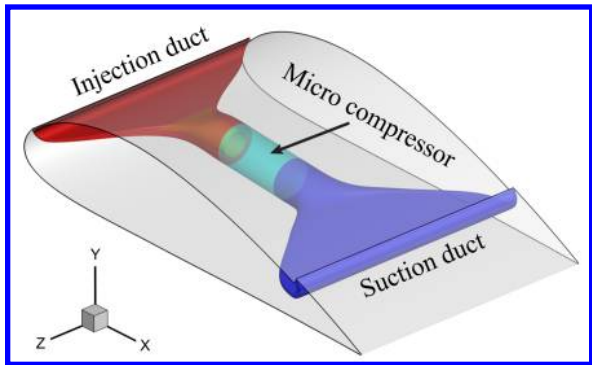


Figure 2: Schematic of CFJ setup within the airfoil

2 Methodology

2.1 Lift and Drag Calculation

In a CFD analysis, the total aerodynamic forces and moments are determined by the force surface integral and jet reactionary force. The reactionary force of a CFJ airfoil is calculated through flow parameters obtained from the injection and suction slots. The equations for lift and drag due to the jet reactionary force are given by Zha et al. [3] using the control volume analysis in Fig. 3:

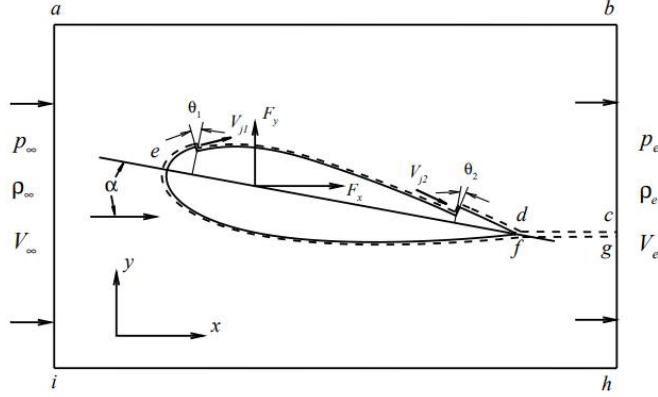


Figure 3: Control volume of a CFJ airfoil

$$F_{x_{cfj}} = (\dot{m}_j V_{j1} + p_{j1} A_{j1}) * \cos(\theta_1 - \alpha) - (\dot{m}_j V_{j2} + p_{j2} A_{j2}) * \cos(\theta_2 + \alpha) \quad (1)$$

$$F_{y_{cfj}} = (\dot{m}_{j1} V_{j1} + p_{j1} A_{j1}) * \sin(\theta_1 - \alpha) + (\dot{m}_{j2} V_{j2} + p_{j2} A_{j2}) * \sin(\theta_2 + \alpha) \quad (2)$$

where the subscript 1 indicates the injection slot and subscript 2 denotes the suction slot, θ_1 and θ_2 are the angles between the slot's surface and a line normal to the chord, and α is the angle of attack.

Total lift and drag are given by the following equations:

$$D = R'_x - F_{x_{cfj}} \quad (3)$$

$$L = R'_y - F_{y_{cfj}} \quad (4)$$

where R'_x and R'_y are surface integrals of pressure and shear stress in the x_{drag} and y_{lift} directions. For a 3D CFJ wing, total lift and drag are determined by integrating the drag and lift equations in the span wise direction.

2.2 Jet Momentum Coefficient

C_μ , or the jet momentum coefficient, quantifies the jet intensity and is defined by,

$$C_\mu = \frac{\dot{m} V_j}{\frac{1}{2} \rho_\infty V_\infty^2 S} \quad (5)$$

where \dot{m} is the injection mass flow rate, V_j is the mass-averaged injection velocity, ρ_∞ is the free stream density, V_∞ is the free stream velocity, and S is the planform area.

2.3 Power Coefficient

In a CFJ airfoil, a system of micro-compressors are embedded inside of the wing. The compressors take air from the suction slot and and eject the air through the injection slot. The power consumption is determined by the jet mass flow and total enthalpy change through:

$$P_{CFJ} = \dot{m}(H_{t1} - H_{t2}) \quad (6)$$

where H_{t1} and H_{t2} are the mass-averaged total enthalpy in the injection and suction slots, P is the power required by the micro-compressor, and \dot{m} the jet mass flow rate. The power required can be expressed by the following equation,

$$P_{CFJ} = \dot{m}C_p T_{t2}(\Gamma^{\frac{\gamma-1}{\gamma}} - 1) \quad (7)$$

where γ is the specific heat ratio, or 1.4 for ideal gas, and η is the isentropic pumping efficiency. Γ is the total pressure ratio of the pump defined as $\Gamma = \frac{P_{t1}}{P_{t2}}$, where P_{t1} and P_{t2} are the mass-averaged total pressures in the injection and suction slots, respectively. The power coefficient for a CFJ airfoil is then,

$$P_{C,CFJ} = \frac{P_{CFJ}}{\frac{1}{2}\rho_\infty V_\infty^3 S} \quad (8)$$

while the actual power coefficient consumed by the micro-compressor is,

$$P_{act} = \frac{P_{C,CFJ}}{\eta} \quad (9)$$

The power coefficient for a propeller actuator is given by,

$$P_P = \frac{2}{\rho V_\infty^3 S} \sqrt{\frac{F^3}{2\rho A}} \quad (10)$$

where F is the total force generated by the propeller actuator perpendicular to the propeller disk, and A is the area of the actuator disk. The propeller power coefficient can also be given by the absolute value of the drag coefficient because the propeller thrust should overcome the drag at cruise.

The power coefficient due to CFJ and the propeller actuator can be combined as,

$$P_C = P_{C,CFJ} + P_P \quad (11)$$

2.4 Corrected Aerodynamic Efficiency

For a conventional wing, the aerodynamic efficiency is defined as:

$$\frac{L}{D} \quad (12)$$

and for a CFJ wing, the pure aerodynamic relationship between lift and drag still follows Eq. 12. However, since CFJ AFC expends energy, the above is modified to consider the energy consumption of the micro-compressor and the propeller actuator. The corrected aerodynamic efficiency is:

$$\frac{C_L}{C_{Dc}} = \frac{C_L}{P_C} = \frac{C_L}{P_P + P_{C,CFJ}} = \frac{C_L}{C_D + P_{C,CFJ}} \quad (13)$$

where C_{Dc} is the equivalent drag coefficient that includes the drag of the aircraft system and the power required by both the propeller and CFJ. At cruise of level and unaccelerated flight, since the propeller thrust exactly offsets the drag, then $C_D = P_P$.

2.5 Aircraft Productivity

The productivity efficiency C_L^2/C_D is used to measure the productivity of an airplane characterized by the product of an aircraft's range and its weight [13]. It is a more thorough parameter than C_L/C_D in determining the merit of aerodynamic design during cruise. Aircraft productivity includes the ratio of lift to drag coefficient and the aircraft weight from C_L . The corrected productivity efficiency for CFJ airfoils with propeller actuator is defined as,

$$\frac{C_L^2}{C_{Dc}} = \frac{C_L^2}{P_C} = \frac{C_L^2}{P_P + P_{C,CFJ}} = \frac{C_L^2}{C_D + P_{C,CFJ}} \quad (14)$$

2.6 Airfoil Geometry

The CFJ airfoil adopted in this paper is developed based on the NACA 6421 airfoil. The CFJ injection and suction slot sizes are normalized by the airfoil chord length (C). The original CFJ airfoil design, CFJ6421-SST150-SUC247-INJ117, created by Wang et. al. [24, 25, 26] is used as a starting point. It has an injection slot size of 1.17%C and suction slot size of 2.47%C. However, during design iterations, the suction slot height is decreased by 30% to reduce flow separation occurring within the duct. The current airfoil used in this study is CFJ6421-SST150-SUC173-INJ117 for Mach numbers 0.17, 0.25, and 0.46.

2.7 Duct Geometry

The ducts have a circular shape at the compressor interface and then become rectangular at the slots. The method of calculating circular-to-rectangular transition surfaces developed in [27] is adopted. The CFJ airfoil injection and suction slot locations are determined according to previously published 2D designs [24, 25, 26]. The injection and suction duct meanlines are determined based on the slot locations. Superellipses are created along the duct meanlines, which pass through the superellipse geometric centers and locally perpendicular to the superellipses. The duct surfaces are formed by connecting those cross sections.

Converging ducts have a favorable pressure gradient and are easier to design than diverging ducts, which are prone to flow separation. When designing the ducts, the center bodies design is important for both the injection and suction duct since they are used to guide the flow entering and exiting the micro-compressor and prevent flow separation. Key parameters in CFJ duct design are the area distribution and the ratio of the slot width to the compressor diameter, W/D .

Duct design is an integral part of the optimization of the system, requiring as high as possible total pressure recovery without flow separation. Total pressure recovery of a CFJ duct is defined as,

$$P_{tr} = \frac{\iint_{S_o} \rho V P_{02} dA}{\iint_{S_i} \rho V P_{01} dA} \quad (15)$$

where S_o and S_i are the cross section interface of the CFJ duct at outlet and inlet respectively. P_{02} and P_{01} are the total pressure evaluated at outlet and inlet. A high total pressure recovery signifies minimal loss within the duct. For injection ducts, the total pressure decreases toward the injection slot while for suction ducts the total pressure decreases toward the compressor interface.

2.8 CFD Simulation Setup

Fig. 2 shows the overall setup for the system integration simulated in this study except that the compressor is not included but is represented by its boundary conditions. The FASIP (Flow-Acoustics-Structure Interaction Package) CFD code is used for the numerical simulation and design. The 3D Reynolds Averaged Navier-Stokes (RANS) equations with one-equation Spalart-Allmaras [17] turbulence model is used. A 3rd order WENO scheme

for the inviscid flux [18, 19, 28, 29, 30, 31] and 2nd order central differencing for the viscous terms [18, 30] are utilized to discretize the Navier-Stokes equations. The low diffusion E-CUSP scheme used as the approximate Riemann solver suggested by Zha et al [19] based on the flux vector-splitting of Zha and Bilgen [32] is utilized with the WENO scheme to evaluate the inviscid fluxes. Implicit time marching method using Gauss-Seidel line relaxation is used to achieve a fast convergence rate [33]. Parallel computing is implemented to save wall clock simulation time [34].

2.9 Boundary Conditions

For the integrated system of Fig. 2, the far field boundary is located at 50 chord lengths. The 3rd order accuracy no slip condition is enforced on the solid surface with the wall treatment suggested in [35] to achieve flux conservation on the wall. Symmetric boundary conditions are utilized on the two boundaries in the span direction. Total pressure, total temperature and flow angles are specified at the injection duct inlet based on the profile of each of the two micro-compressors at the outlet. The total pressure, total temperature, and flow angle are also specified at the upstream portion of the far field based on free stream condition. Constant static pressure is applied at the suction duct outlet as well as the downstream portion of the far field. The actuator disk boundary condition is modeled as a flat surface with a pressure jump, which is iterated so that the sum of forces in the free stream (x) direction is 0. The total mesh size for the CFJ airfoils at Mach number 0.17 and 0.25 is 5.68 million points, split into 135 blocks for the parallel computation. The total mesh size for the CFJ airfoil at Mach number 0.46 is 5.81 million points, split into 139 blocks for the parallel computation. The first grid point on the wing surface is placed at $y^+ \approx 1$.

2.10 Procedure for the Integrated Design

The integrated design procedure is described as the following steps illustrated in the chart of Fig. 4. But in this study, Step 2 of the micro-compressor is only done once and is not in the iteration.

1. CFJ wing design: 2D CFJ airfoil and 3D CFJ wing are designed to meet the aircraft mission requirements for takeoff, cruise, and landing with optimal performance. The design provides the requirements of wing dimensions, micro-compressor mass flow rate, and total pressure ratio.
2. Micro-compressor design: A micro-compressor is then designed to satisfy the required total pressure ratio and the dimensions of the airfoil with maximized mass flow rate, highest efficiency, and largest operating range from choke limit to stall limit.
3. Duct design: The CFJ injection and suction ducts are then designed to match the airfoil dimensions with the boundary conditions from the micro-compressor and the CFJ wing flow conditions, no flow separation inside the ducts, and minimum total pressure loss.
4. Integrate the ducts with the 3D CFJ airfoil using the micro-compressor flow conditions at the CFJ injection inlet (micro-compressor outlet) and suction outlet (micro-compressor inlet). Simulate the 3D CFJ airfoil with the ducts designed in Step 3.
5. Examine the results and the aerodynamic performance. If satisfied, stop; if not satisfied, return to Step 1 and repeat the process. However, to save time, Step 2 of the compressor design is not iterated in this study and is only conducted at the beginning. Thus the micro-compressor is a quasi-micro-compressor.

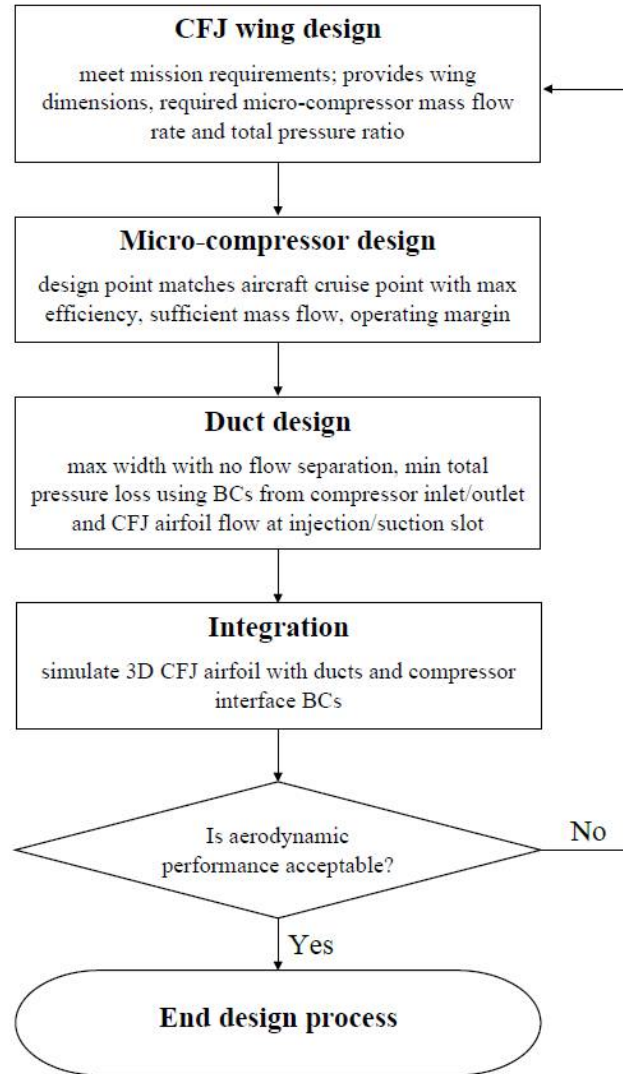


Figure 4: Flowchart of the integrated design process

3 Results and Discussion

3.1 The Micro-Compressors

Three cruise Mach numbers are studied in this paper to achieve high power conversion efficiency: 0.17, 0.25, and 0.46. The function of the micro-compressor actuator is to provide the mass flow and jet momentum required by CFJ flow control. Once the airfoil is designed by CFD simulation, the required mass flow and total pressure ratio between the suction outlet and injection inlet will be used as the performance requirements to design the micro-compressor. The total pressure ratio is determined by the energy loss in the jet mixing with the main flow. A higher free stream Mach number will create a greater loss at the same AoA and C_{μ} because the high speed will have more shear stress work on the surface. For Mach numbers 0.17 and 0.25, the total pressure loss is small and the total pressure ratio required for the micro-compressor at cruise condition is about 1.015. For Mach 0.46, the required total pressure ratio is 1.15. They are at quite different range. To be efficient for each system, two micro-compressors are designed, namely G8A for Mach numbers 0.17 and 0.25, and G5 for Mach number 0.46.

The following table summarizes the design point performance for each compressor.

Table 1: Design point performance of micro-compressors G8A and G5

	Mach	$\dot{m}(kg/s)$	P_{tr}	η
G8A	0.17, 0.25	0.1650	1.04	84%
G5	0.46	0.1706	1.17	78.6%

3.2 CFJ Injection and Suction Ducts

In order to integrate the micro-compressors with the CFJ airfoil, the injection and suction ducts must be designed according to the following:

1. Match the mass flow requirement for the required C_μ .
2. No flow separation inside the ducts to minimize total pressure loss and maximize flow uniformity at the injection slot.
3. Maximize slot width to minimize the number of micro-compressors to be used. However, a large ratio of slot width to compressor diameter, W/D , will also make the flow easier to separate.

For the three Mach numbers studied, in each the injection duct has a converging area variation while the suction duct has a diverging area variation.

3.2.1 $M = 0.17$

The ducts designed for $M = 0.17$ have a width to diameter (W/D) ratio of 3.36 for both injection and suction ducts to match the G8A micro-compressor diameter at the inlet and outlet. Fig. 5 shows the mesh used for the ducts and the suction surface of the airfoil, each duct has a mesh size of 1.62 million points, split into 20 blocks for parallel computation. The total mesh size of the 3D domain is 5.68 million points, split into 135 blocks. The injection and suction ducts have a total pressure recovery of 99.05% and 99.55% respectively, shown in Fig. 6.

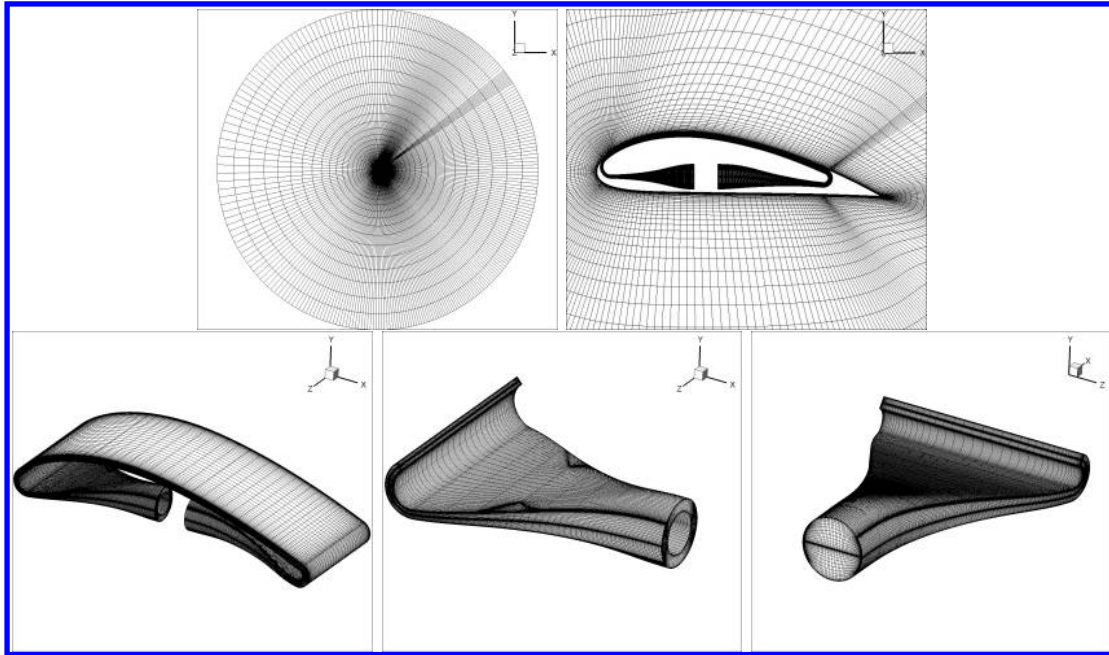


Figure 5: Computational mesh of airfoil surfaces and ducts used for $M = 0.17$

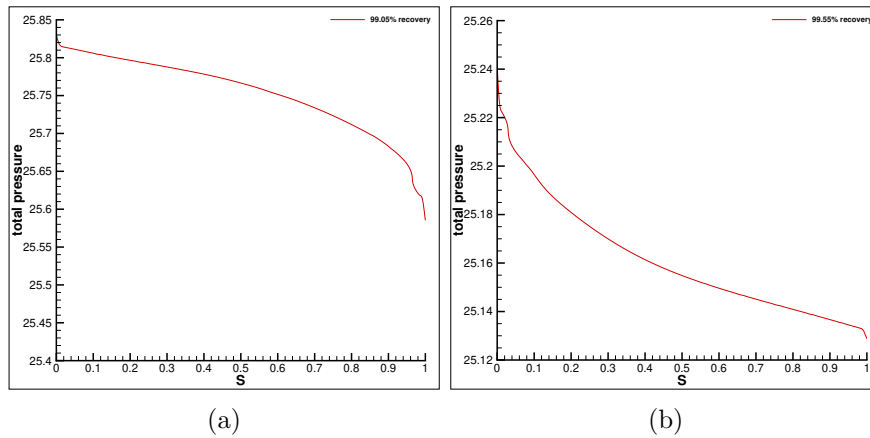


Figure 6: Total pressure distribution for (a) injection and (b) suction duct designed for the CFJ airfoil using G8A micro-compressor at Mach number 0.17

Mach contours and streamlines are shown in Fig. 7 for the injection and suction ducts. Contours of the injection duct show at the compressor interface the sides of the center body having a stronger flow than the top and bottom. This is caused by the swirl effect on the flow from the G8A micro-compressor. The flow is attached throughout the span of the injection duct. The suction duct shows very healthy flow throughout except at the top of the duct near the micro-compressor interface where there is a low Mach number region. However, the streamlines do not show any separation and with such a high total pressure recovery, the design is acceptable.

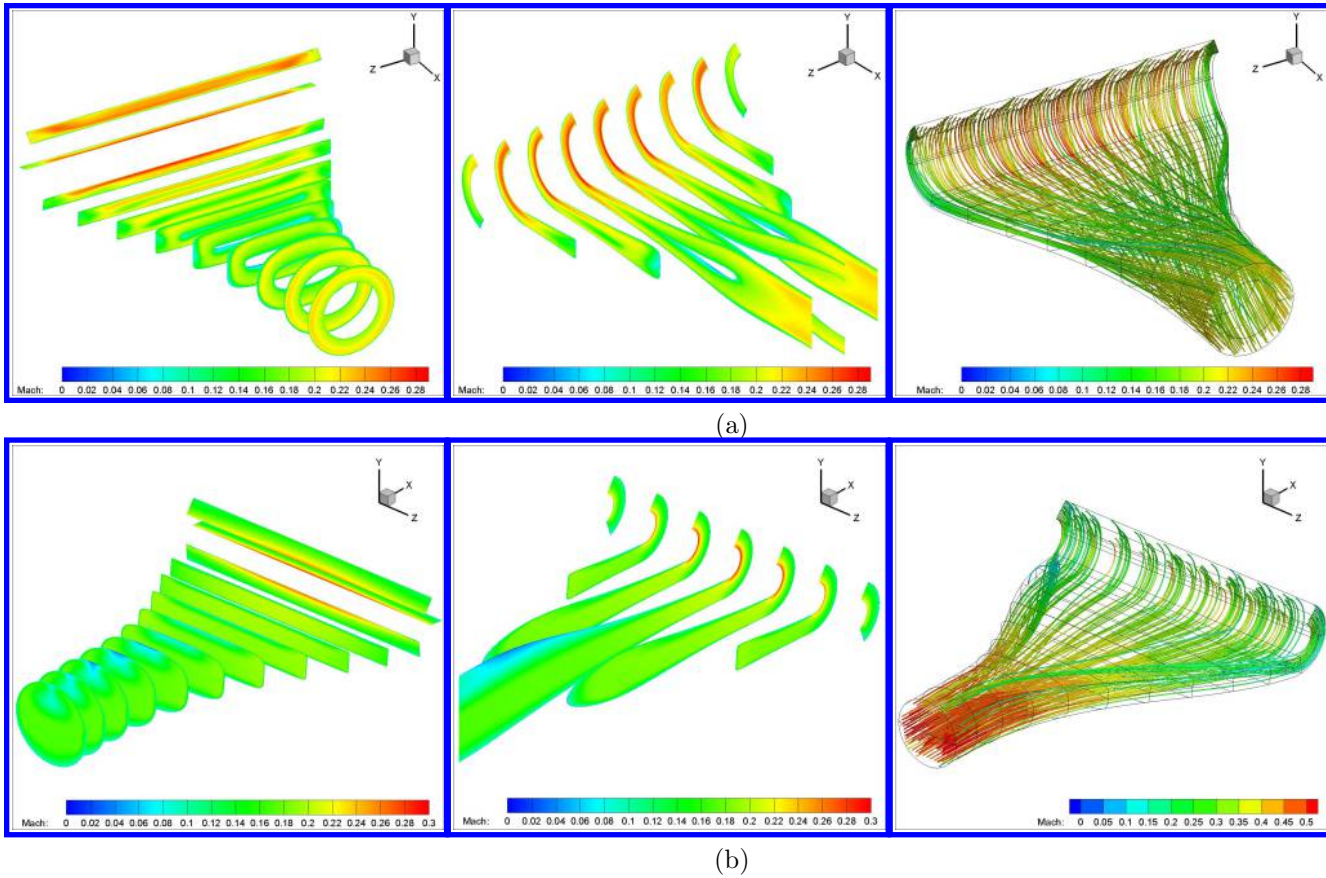


Figure 7: Mach contours and streamlines at (a)injection and (b)suction for CFJ airfoil using G8A micro-compressor at Mach number 0.17

3.2.2 $M = 0.25$

Both injection and suction ducts designed for $M = 0.25$ have a W/D ratio of 2.76. That is because the inlet and outlet diameters of G8A micro-compressor are equal. Fig. 8 shows the mesh used for both ducts and the suction surface of the airfoil. Each duct has a mesh size of 1.62 million points, split into 20 blocks. The total mesh size for the 3D domain is 5.68 million points, split into 135 blocks. The injection and suction ducts have a total pressure recovery of 98.78% and 99.1% respectively, shown in Fig. 9.

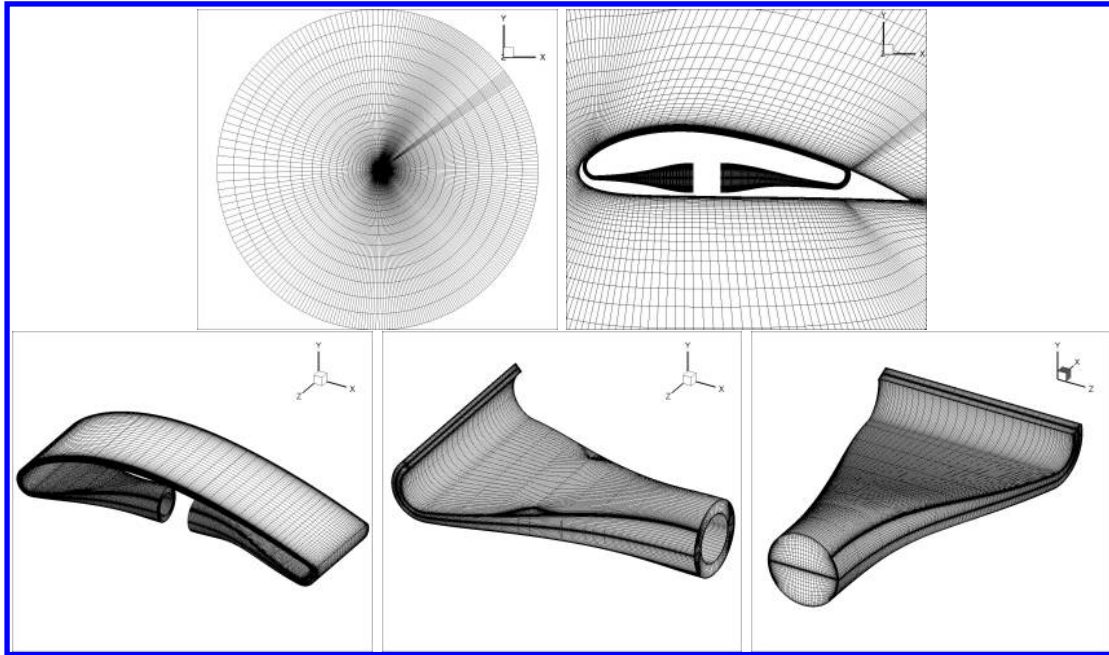


Figure 8: Computational mesh of airfoil surfaces and ducts used for $M = 0.25$

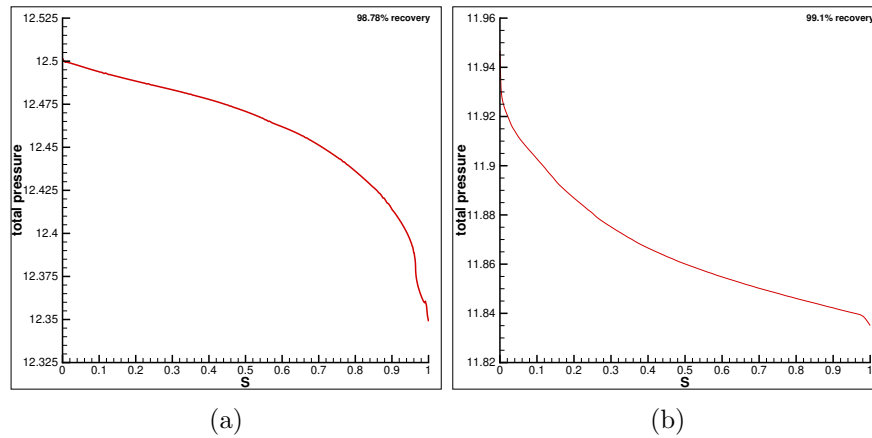


Figure 9: Total pressure distribution for (a) injection and (b) suction duct designed for CFJ airfoil using G8A micro-compressor at Mach number 0.25

Mach contours and streamlines are shown in Fig. 10 for the injection and suction ducts. Contours of the injection duct show the flow is attached throughout the duct with the Mach number at the injection slot fairly uniform. The streamlines clearly display the swirl effects due to the micro-compressor G8A. The suction duct shows very healthy flow throughout. Flow is generally strong in the majority area of the duct because of the centrifugal forces at the turn near the inlet that push flow to the bottom. At the top of the duct near the micro-compressor interface there is a very small low Mach number region. Upon further inspection of the design suction duct, however, the streamlines do not show any separation. The suction designed is deemed acceptable to continue with due to the high total pressure recovery.

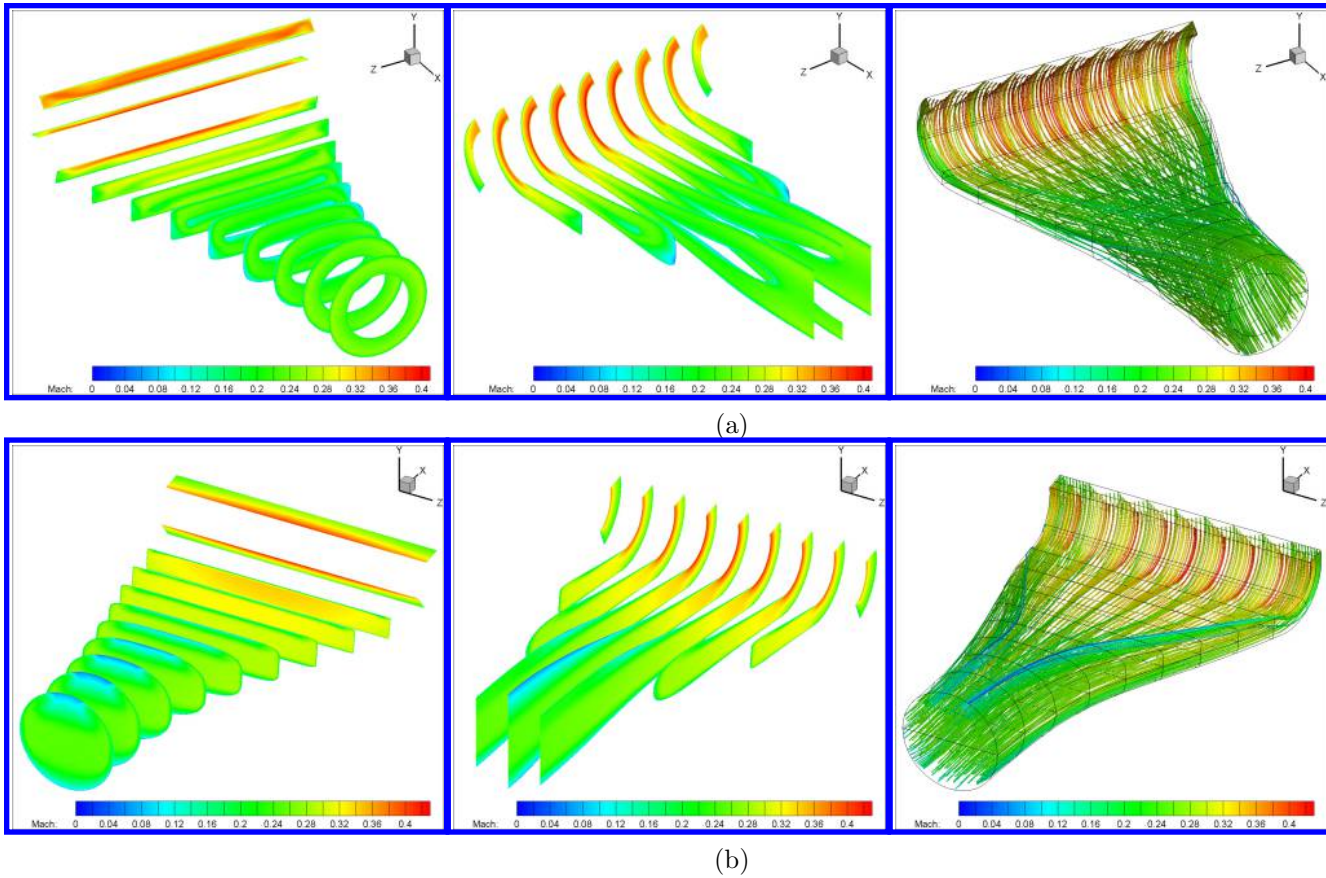


Figure 10: Mach contours and streamlines at top row: injection duct, bottom row: suction duct, for CFJ airfoil using G8A micro-compressor at Mach number 0.25

3.2.3 $M = 0.46$

For $M = 0.46$, Fig. 11 shows the mesh used for the ducts and the suction surface of the airfoil. W/D for injection duct is 1.47 and has a mesh size of 1.68 million points, split into 24 blocks. The suction duct has a W/D of 2.23 and a mesh size of 1.62 million points, split into 20 blocks. The width to diameter ratio differs for both ducts because the micro-compressor G5 design has a smaller inlet and larger outlet. The total pressure distribution of Fig. 12 shows the injection duct has a recovery of 96.32% while the suction duct has a total pressure recovery of 97.78%. The injection duct total pressure recovery is significantly lower than that at lower free stream Mach number of 0.17 and 0.25. This is because the injection jet speed is substantially higher for Mach number 0.46 as can be seen by comparing the Mach contours in Fig. 13 with those in Fig. 7 and 10. A high speed jet will create more total pressure loss.

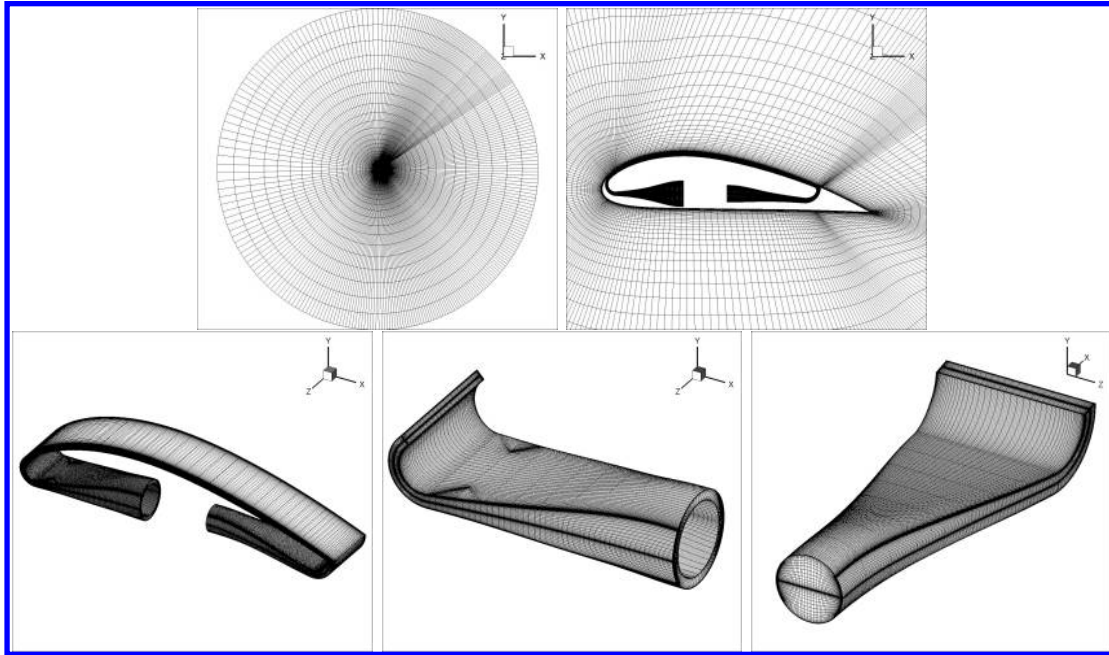


Figure 11: Computational mesh of airfoil surfaces and ducts used for $M = 0.46$

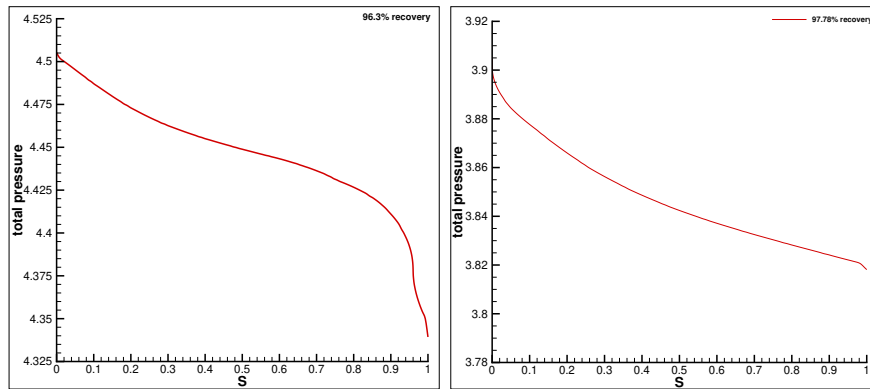


Figure 12: Total pressure distribution for (a) injection and (b) suction duct designed for CFJ airfoil using G5 micro-compressor at Mach number 0.46

Mach contours and streamlines show the flow within the ducts in Fig. 13. The injection duct shows healthy flow throughout the duct despite the low pressure recovery. The flow at the injection slot is rather uniform. Streamlines depict the swirl from the micro-compressor G5. The suction duct contours indicate a strong flow throughout the duct as well. At the compressor interface the flow seems just slightly lower at the top and bottom of the duct compared to the center flow but it is not nearly as low as the previous Mach numbers studied. The streamlines do not show any separation.

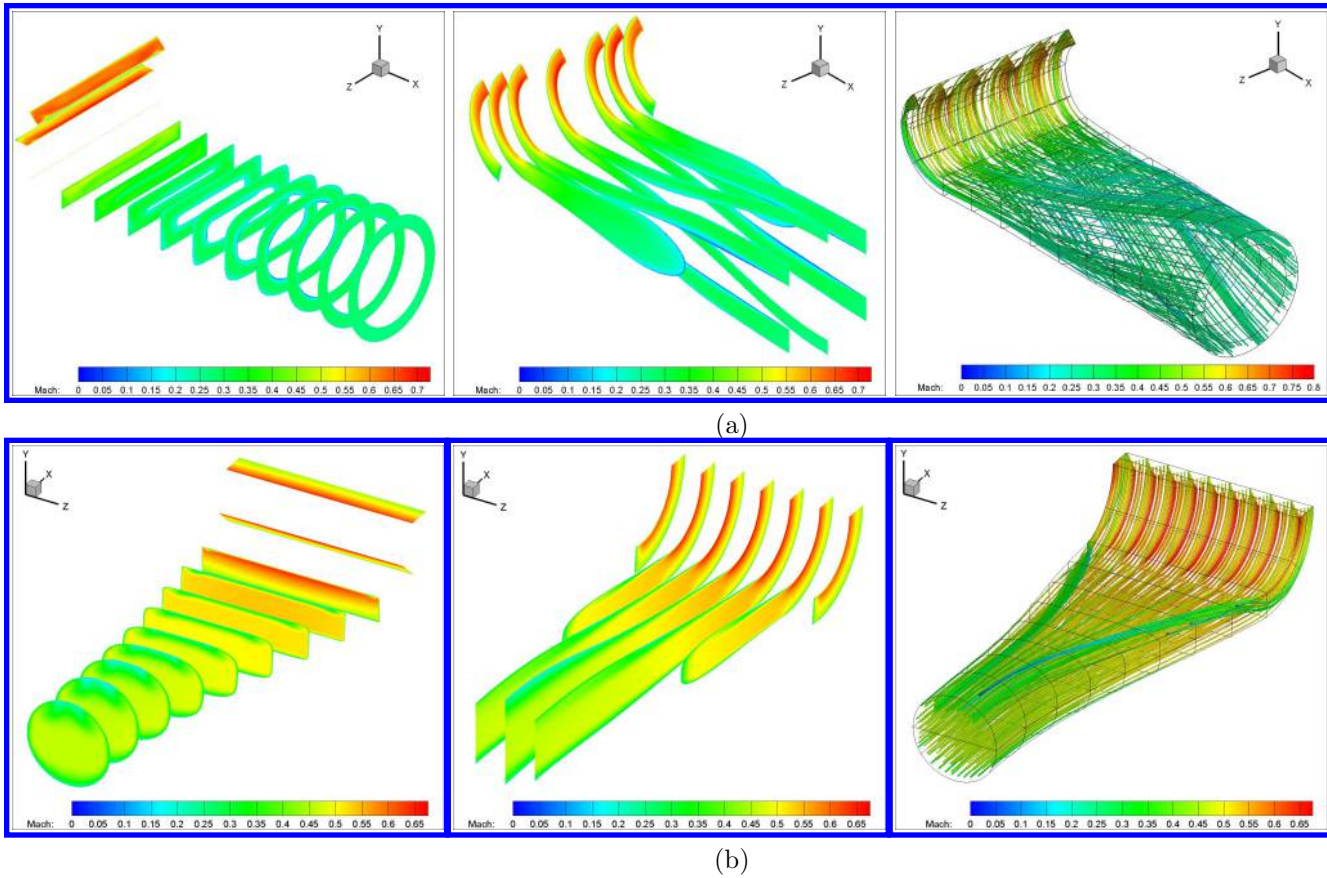


Figure 13: Mach contours and streamlines at (a)injection and (b)suction for CFJ airfoil using G5 micro-compressor at Mach number 0.46

3.3 Integration of the Micro-Compressors with CFJ Airfoil

Once the duct designs for all three Mach numbers is completed, they are incorporated into the 3D CFJ airfoil and the flow field is simulated with the external flow and the internal duct flow. The results of the numerical simulation analysis are shown below for each micro-compressor. Angles of attack 0° through 5° were simulated at a C_μ of 0.03 as per [26, 36], however, at higher AoA the jet momentum coefficient had to be increased to remove flow separation occurring on the suction surfaces. Values of P_C indicate the total power coefficients of the CFJ airfoil ($P_{C,CFJ}$) and the propeller actuator (P_P). In the following Tables 2 and 3, the value of the propeller actuator power coefficient P_P is equivalent to the drag coefficient C_D , as previously concluded.

3.3.1 G8A Micro-Compressor

Table 2 lists the performance of cruise Mach numbers 0.17 and 0.25 at different angles of attack, 0° to 15° using the G8A micro-compressor. The value of C_L/C_D follows conventional aerodynamic performance definition of Eq. 12, but in this case C_D is equal to the propeller actuator power coefficient P_P since at cruise of level and unaccelerated flight, the propeller thrust exactly offsets the drag. The highest CFJ corrected aerodynamic efficiency C_L/C_{Dc} , occurs at angle of attack 5° for both Mach numbers: 58.04 at $M = 0.17$ and 74.09 at $M = 0.25$. These are similar to the results observed by Wang et al. [26] for a 2D CFJ airfoil simulation using rectangular ducts at Mach numbers 0.15 and 0.3.

At every flow condition of AoA and C_μ , the simulation gives the compressor mass flow rate and the total

pressure ratio, which are then plotted on the compressor map in Fig. 14. The compressor map is an output of the compressor with the compressor efficiency contours superimposed. From the map, we can see the compressor working condition, including the compressor efficiency, how far from the stall boundary and choked boundary. If the CFJ airfoil does not work at the desirable efficiency region, the duct can be redesigned in the overall iteration and the compressor can be redesigned too. The results shown in this section are from the final designs after the design iterations shown in Fig. 4. The G8A micro-compressor will work at an operating point with an efficiency of 76% for the Mach number 0.17 cruise point and at 79% for Mach number 0.25 cruise condition, a very desirable performance. For all angles simulated, the G8A micro-compressor performs at an efficiency range of 76% to 82% for Mach number 0.17 and 78% to 85% for Mach number 0.25.

Table 2: Performance at $M = 0.17$ and $M = 0.25$ for different AoA with G8A micro-compressor

Mach	AoA	C_μ	C_L	PP^*	$P_{C,CFJ}$	P_C	C_L/C_D	C_L/C_{Dc}	C_L^2/C_{Dc}	P_{tr}	\bar{m}	η
0.17	0°	0.03	0.770	0.0066	0.0170	0.0237	117.37	32.58	25.10	1.025	0.828	82%
	2.5°	0.03	1.033	0.0083	0.0131	0.0213	128.75	48.41	49.98	1.019	0.815	78%
	5°	0.03	1.246	0.0118	0.0097	0.0215	105.37	58.04	72.33	1.014	0.807	76%
	7.5°	0.05	1.588	0.0118	0.0215	0.0334	134.81	47.56	75.51	1.025	1.037	78%
	10°	0.07	1.901	0.0132	0.0364	0.0497	143.33	38.28	72.76	1.036	1.217	78%
	12.5°	0.10	2.271	0.0129	0.0606	0.0735	176.84	30.90	70.19	1.051	1.448	80%
	15°	0.12	2.556	0.0161	0.0849	0.1011	157.96	25.29	64.63	1.066	1.579	81%
0.25	0°	0.03	0.825	0.0040	0.0156	0.0196	192.53	42.02	34.66	1.051	1.017	84%
	2.5°	0.03	1.101	0.0057	0.0119	0.0176	193.50	62.54	68.86	1.039	1.009	85%
	5°	0.03	1.321	0.0098	0.0080	0.0178	134.02	74.09	97.85	1.027	0.996	79%
	7.5°	0.03	1.446	0.0195	0.0062	0.0258	74.05	56.09	81.09	1.021	0.985	78%
	10°	0.07	1.990	0.0104	0.0267	0.0371	191.52	53.68	106.83	1.061	1.468	82%
	12.5°	0.10	2.365	0.0100	0.0447	0.0547	240.16	43.25	102.31	1.088	1.720	82%
	15°	0.12	2.649	0.0128	0.0573	0.0701	206.06	37.79	100.09	1.106	1.842	83%

Fig. 14 shows the compressor map at different RPM of the G8A micro-compressor along with the operating conditions of the CFJ airfoil at Mach numbers 0.17 and 0.25 at different AoA labeled in the circles and different C_μ as reflected in Table 2. For a constant C_μ at Mach 0.17 with AoA = 0 – 5° and Mach 0.25 with AoA = 0 – 7.5°, as AoA increases, the total pressure ratio decreases and the mass flow slightly decreases because the jet velocity is slightly increased due to the higher leading edge suction peak effect. Starting from AoA of 0°, the total pressure ratio decreases with the increasing AoA first since the flow is well attached with the decreasing suction peak pressure, which requires less pumping power [9]. But, when the C_μ is increased for higher angles of attack, the mass flow rate along with the total pressure ratio increase. When the AoA is beyond 5° at Mach 0.17 and 7.5° at Mach 0.25, the total pressure is increased because the CFJ requires more power to overcome the adverse pressure gradient [9]. The operating conditions of the CFJ airfoil at $M = 0.17$ and $M = 0.25$ all fall within the high efficiency operating range of the G8A micro-compressor and show that the integrated system can operate at a high compressor efficiency.

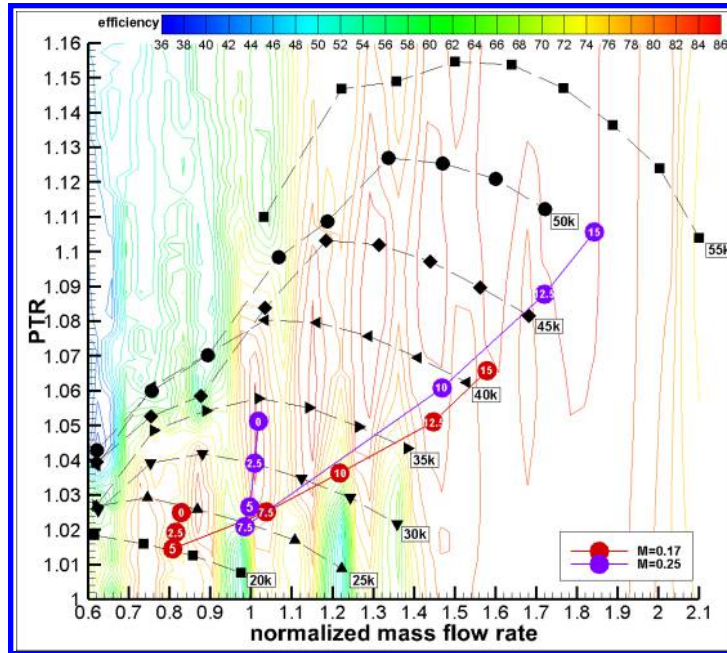


Figure 14: Compressor map of G8A micro-compressor with operating conditions of CFJ airfoil at different AoA labeled in the circles for Mach numbers 0.17 and 0.25

The flow field of the CFJ airfoil at the 50% span wise location for AoA 5° for $M = 0.17$ is shown in Fig. 15(a). The maximum Mach number in the flow field reaches 0.28. The flow field is well attached to the airfoil. The suction surface shows some flow non-uniformity that is created by the swirl flow coming out of the G8A micro-compressor. Still, the overall flow performs very well. The Mach contours at 50% span show the suction duct having a small low Mach number region at the top of the middle section of the duct, but the streamlines do not show any flow separation. Fig. 15(c) and (d) show flow from the free stream far field (color streamlines) merges with the flow from the injection duct (black streamlines) and both go into the suction duct. The flow in the suction duct is mixed between the injection jet and the main flow. The flow from the main stream (color streamlines) is more concentrated at the bottom and the edges of the suction duct due to the centrifugal force at the turn of the suction duct, while the injection jet (black streamlines) tends toward the center of the suction duct due to lower momentum of the airfoil boundary layer.

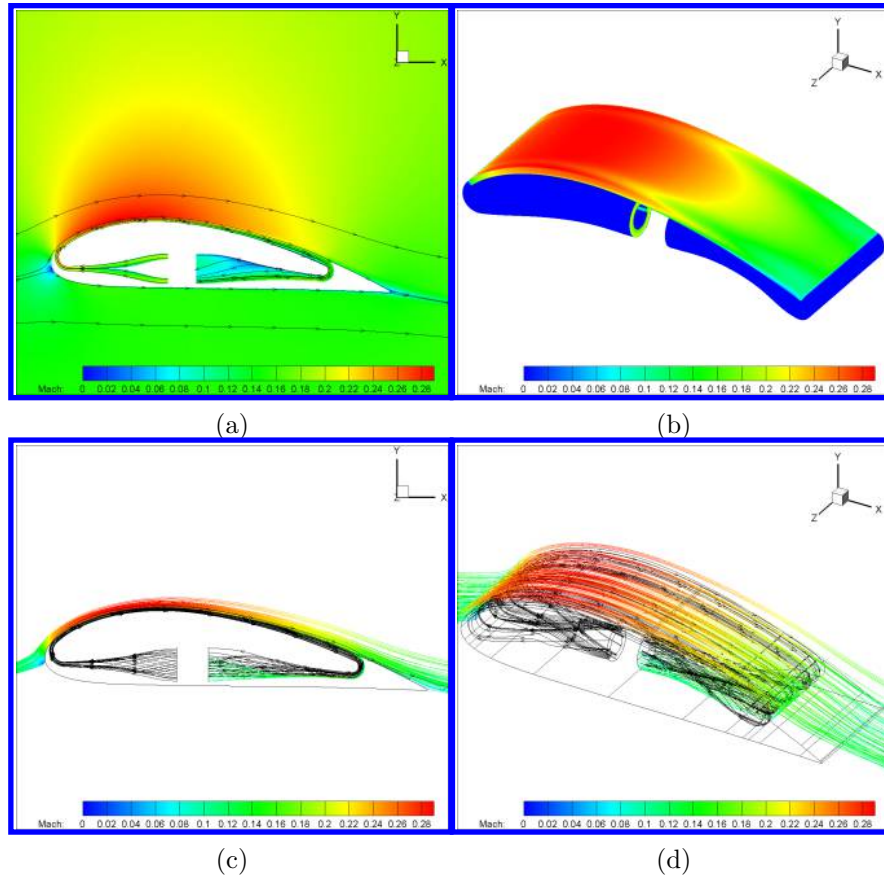


Figure 15: (a)Mach contour flow field of the CFJ airfoil at 50% span wise location and (b)mach contour of designed ducts and suction surface, (c) and (d)far field and injection duct streamlines merging into suction duct at AoA 5° and with G8A micro-compressor for $M = 0.17$

The flow field of the CFJ airfoil at the 50% span wise location for AoA 5° for Mach number 0.25 is shown in Fig. 16(a). The maximum Mach number in the flow field reaches 0.42. The flow field is well attached to the airfoil throughout. The suction surface shows some flow non-uniformity, created by the swirl flow coming out of the G8A micro-compressor. However, overall the flow performs very well. The Mach contours at 50% span show the suction duct outlet having a low Mach number region at the top half of the duct, but the streamlines along the ducts and suction surface do not show any flow separation. Fig. 16(c) and (d) show some of the flow from the far stream far field (color streamlines) merges with the flow from the injection duct (black streamlines) and both go into the suction duct. The flow going into the suction duct is mixed between the injection jet and the main flow as shown by the streamlines in black and in color. A comparison of Fig. 16(c) and (d) shows that the flow from the injection jet is more on the top of the suction duct with low energy due to the boundary layer loss (black streamlines), whereas the flow from the main stream is more thrown to the bottom of the duct (color streamlines) due to the centrifugal force at the turning of the suction duct.

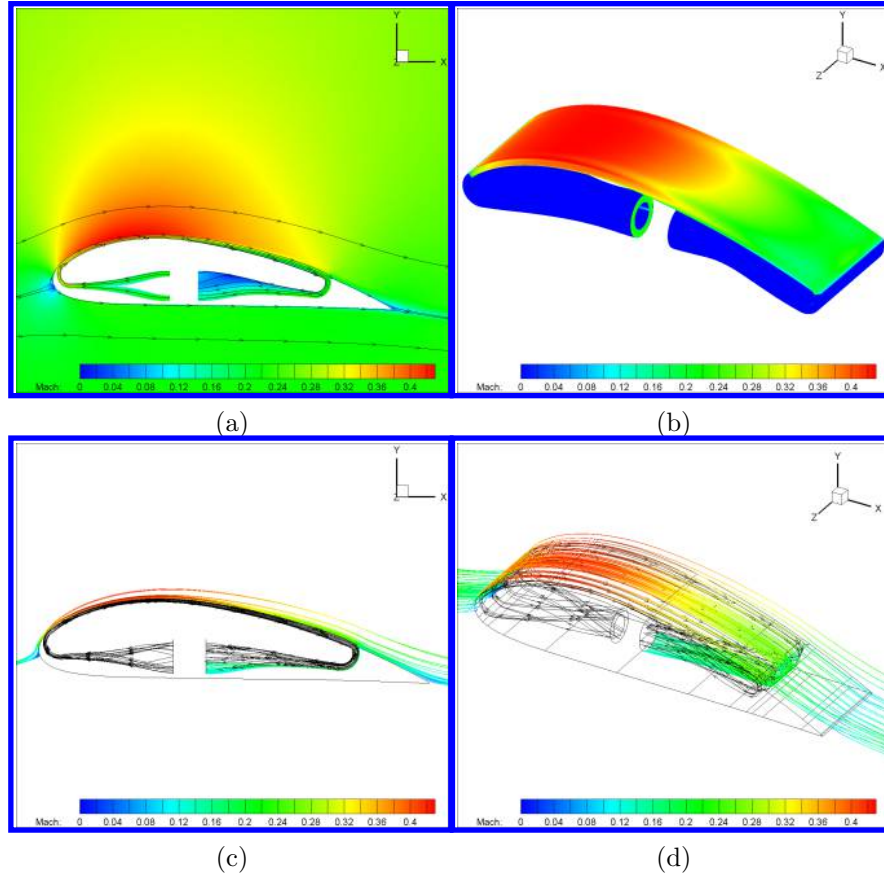


Figure 16: (a)Mach contour flow field of the CFJ airfoil at 50% span wise location, (b)mach contour of designed ducts and suction surface, (c) and (d)far field and injection duct streamlines merging into suction duct at $AoA=5^\circ$ with G8A micro-compressor for $M = 0.25$

3.3.2 G5 Micro-Compressor

Table 3 lists the performance of cruise Mach number 0.46 at different angles of attack, 0° to 10° using G5 micro-compressor. Higher angles of attack could not be achieved due to separation on the suction surface. The value of C_L/C_D follows Eq. 12, but C_D is equal to the propeller actuator power coefficient P_P since at cruise of level and unaccelerated flight, the propeller thrust exactly offsets the drag. The highest CFJ corrected aerodynamic efficiency occurs at $AoA 5^\circ$, 76.26. This is within 2% of the results obtained by Wang et al. [26] for a 2D CFJ airfoil with rectangular ducts at Mach number 0.46. G5 micro-compressor will operate at a cruise efficiency of 76%, also a very high level. For the angles simulated, the G5 micro-compressor performs at efficiency higher than 66%, lower than the previous Mach numbers studied but still a good performance.

Fig. 17 shows the compressor map at different RPM of the G5 micro-compressor along with the operating conditions of the CFJ airfoil at Mach number 0.46. For the same C_μ , as AoA increases from 0° to 5° , the mass flow rate decreases because the jet velocity is increased due to the higher leading edge suction peak effect, and the total pressure ratio also decreases as explained for Fig. 14. With C_μ increased to 0.05 for $AoA 7.5^\circ$ and 0.07 for 10° , the mass flow rate and the total pressure ratio increase. At 7.5° the CFJ operating point falls within the micro-compressor map, but the flow over the airfoil reaches supersonic speeds with increased total pressure loss and thus compressor power. At 10° the CFJ airfoil operating condition falls outside of the operating conditions of the G5 compressor map. This is because the flow over the airfoil reaches supersonic speeds with a normal shock wave, which creates a large loss due to the shock boundary layer interaction. The high loss requires a high total

Table 3: Performance at $M = 0.46$ different AoA with G5 micro-compressor

Mach	AoA	C_μ	C_L	P_P	$P_{C,CFJ}$	P_C	C_L/C_D	C_L/C_{Dc}	C_L^2/C_{Dc}	P_{tr}	\bar{m}	η
0.46	0°	0.03	0.944	0.0047	0.0166	0.0213	187.20	43.69	41.26	1.187	1.055	77%
	2°	0.03	1.201	0.0054	0.0141	0.0196	215.51	60.90	73.15	1.164	1.017	78%
	2.5°	0.03	1.261	0.0058	0.0135	0.0194	214.50	64.95	81.88	1.158	1.007	78%
	5°	0.03	1.514	0.0096	0.0103	0.0199	158.91	76.26	115.42	1.125	0.958	76%
	7.5°	0.05	1.948	0.0091	0.0206	0.0298	212.38	65.35	127.30	1.212	1.165	73%
	10°	0.07	2.333	0.0175	0.0449	0.0625	133.20	37.36	87.14	1.416	1.364	66%

pressure ratio and compressor power beyond the range that the compressor is designed. In other words, at the cruise condition of Mach 0.46 using the G5 micro-compressor, the aircraft should avoid AoA greater than 10°, or the micro-compressor needs to be redesigned to have a larger range. For all other angles of attack, the operating conditions of the CFJ airfoil at $M = 0.46$ fall within the high efficiency operating range of the G5 micro-compressor and show that the integrated system can operate at high compressor efficiency.

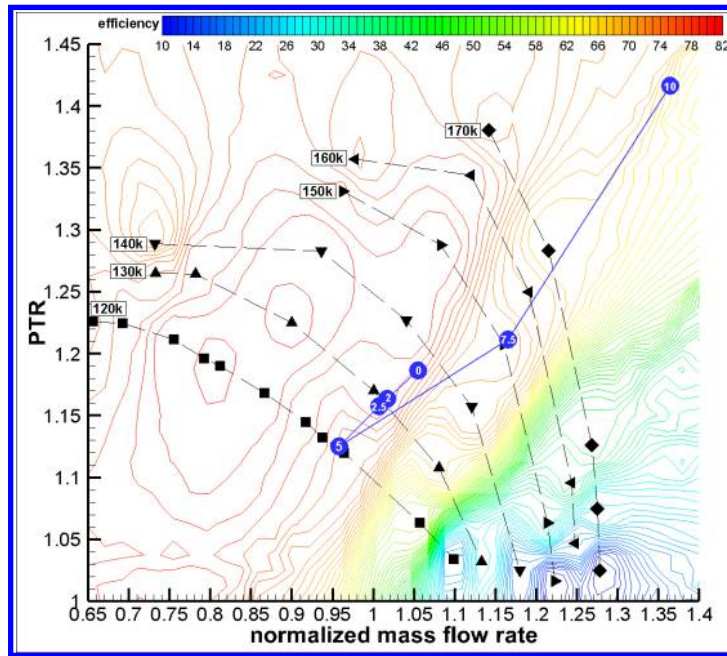


Figure 17: Compressor map of G5 micro-compressor with operating conditions of CFJ airfoil at different AoA for Mach number 0.46

Fig. 18(a) shows the flow field of the CFJ airfoil at 50% span wise location for AoA 5° for Mach 0.46. It clearly shows the difference in diameters of the G5 compressor inlet and outlet. The maximum Mach number in the flow field is 0.95. The flow field is well attached to the airfoil. The ducts and suction surface show a healthy flow from the injection duct towards the suction duct, however there is non-uniformity from the swirl effect of the G5 micro-compressor. The Mach contours at 50% span show the suction duct having a low Mach number region at the top of the suction duct outlet, but the streamlines do not show any flow separation. Fig. 18(c) and (d) show some of the main flow from the far stream far field (color streamlines) merges with the flow from the injection duct jet (black streamlines) and the mixed flow go into the suction duct. The flow from the injection jet is focused on the center of the suction duct with low energy due to boundary layer loss (black streamlines), whereas the flow

from the main stream is more thrown to the bottom of the duct (color streamlines) due to the centrifugal force at the turning of the suction duct. Some of the main flow is also the cause for the weak flow at the top of the suction duct, from Fig. 18(a).

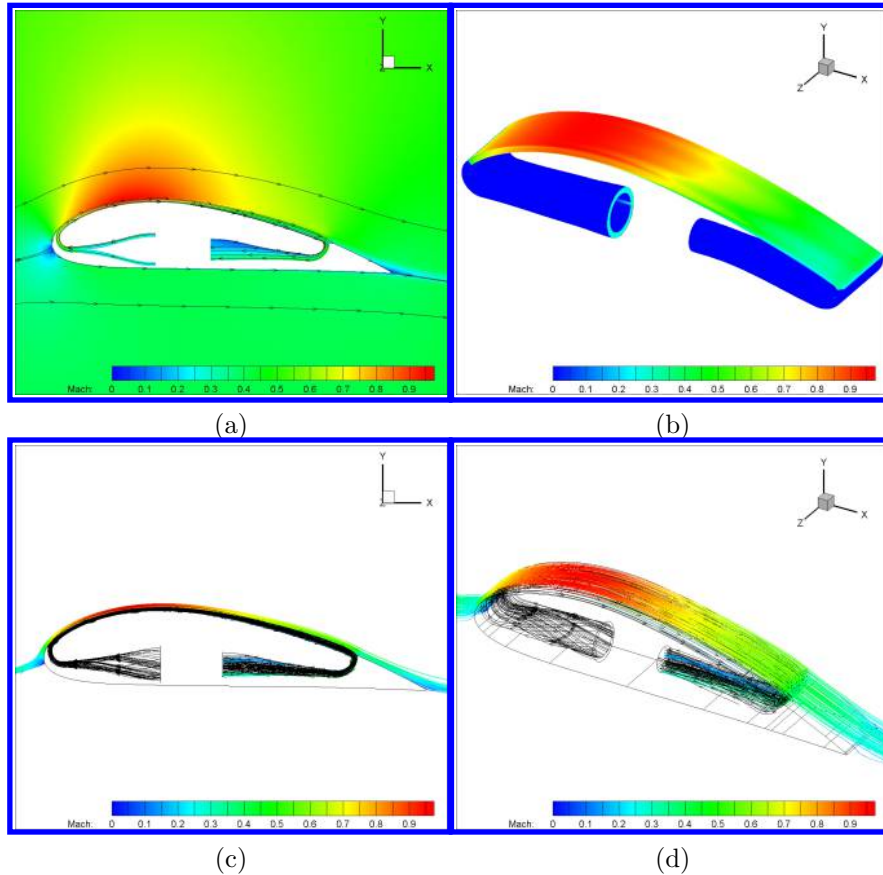


Figure 18: (a)Mach contour flow field of the CFJ airfoil at 50% span wise location and (b)mach contour of designed ducts and suction surface, (c) and (d)far field and injection duct streamlines merging into suction duct at at AoA 5° and with G5 micro-compressor for $M = 0.46$

4 Conclusion

This paper conducts a design study for a 3D Co-Flow Jet (CFJ) airfoil with an integrated quasi-micro-compressor represented by boundary conditions. At Mach numbers 0.17 and 0.25 the G8A micro-compressor is used, while at Mach number 0.46 the G5 micro-compressor is utilized. The purpose is to let the micro-compressor operate at the high efficiency range at the cruise condition. For all the Mach numbers, the cruise AoA is 5° . First in the design process, the CFJ airfoil is designed for optimal cruise efficiency meeting the mission requirements. Second, a micro-compressor is designed to satisfy required total pressure and the airfoil dimensions with a maximized mass flow rate. The micro-compressor in this study is not redesigned in the design iteration. Its boundary conditions are used to represent the micro-compressor at the interface with the CFJ airfoil. Thirdly, injection and suction ducts are designed iteratively to have minimal total pressure loss and match the high efficiency operating region of the compressor map. The ducts have a circular shape at the micro-compressor interface and transition to rectangle slots at the airfoil. Duct design is crucial in the integration of the CFJ airfoil with the micro-compressor, by matching the mass flow rate and compressor total pressure ratio to the high efficiency operating region. The micro-compressor outlet is simulated with a swirl profile boundary condition provided from each of the compressor

designs. The cruise condition is angle of attack 5° with a range from 0° to 15° . Results show that by integrating a micro-compressor and CFJ airfoil through duct design, an operating range at cruise for the CFJ airfoil system is achieved with excellent micro-compressor efficiency. For $M = 0.17$ and G8A micro-compressor the efficiency range is 76% to 82%, for $M = 0.25$ and G8A micro-compressor the efficiency range is 79% to 85%, and for $M = 0.46$ and G5 micro-compressor the efficiency range is 73% to 78%. Therefore, an integrated system design of CFJ airfoil and micro-compressor results in the CFJ aircraft cruising at a high efficiency operating range of the compressor for a range of Mach numbers.

5 Acknowledgement

The authors would like to acknowledge the computing resources provided by the Center of Computational Sciences (CCS) at the University of Miami. The teaching assistantship support from the University of Miami is also acknowledged.

Disclosure: The University of Miami and Dr. Gecheng Zha may receive royalties for future commercialization of the intellectual property used in this study. The University of Miami is also equity owner in CoFlow Jet, LLC, licensee of the intellectual property used in this study.

References

- [1] K. Xu, Y. Ren, and G.-C. Zha, "Numerical analysis of energy expenditure for co-flow wall jet separation control." AIAA SciTech 2022, San Diego, CA, Accepted for publication in AIAA Journal, 2022, 3 - 7 Jan 2022.
- [2] G. Zha, and C.D. Paxton, "A Novel Flow Control Method for Airfoil Performance Enhancement Using Co-Flow Jet," *Applications of Circulation Control Technologies, AIAA Book Series, Progress in Aeronautics and Astronautics*, vol. Vol. 214, Chapter 10, pp. 293–314, 2006.
- [3] G. Zha, W. Gao, and C.D. Paxton, "Jet Effects on Co-Flow Jet Airfoil Performance," *AIAA Journal*, vol. 45, pp. 1222–1231, 2007.
- [4] G.-C. Zha, C. Paxton, A. Conley, A. Wells, and B. Carroll, "Effect of Injection Slot Size on High Performance Co-Flow Jet Airfoil," *AIAA Journal of Aircraft*, vol. 43, pp. 987–995, 2006.
- [5] G.-C. Zha, B. Carroll, C. Paxton, A. Conley, and A. Wells, "High Performance Airfoil with Co-Flow Jet Flow Control," *AIAA Journal*, vol. 45, pp. 2087–2090, 2007.
- [6] Wang, B.-Y. and Haddoukessouni, B. and Levy, J. and Zha, G.-C., "Numerical Investigations of Injection Slot Size Effect on the Performance of Co-Flow Jet Airfoil," *Journal of Aircraft*, vol. Vol. 45, No. 6., pp. pp.2084–2091, 2008.
- [7] B. P. E. Dano, D. Kirk, and G.-C. Zha, "Experimental Investigation of Jet Mixing Mechanism of Co-Flow Jet Airfoil." AIAA-2010-4421, 5th AIAA Flow Control Conference, Chicago, IL, 28 Jun - 1 Jul 2010.
- [8] B. P. E. Dano, G.-C. Zha, and M. Castillo, "Experimental Study of Co-Flow Jet Airfoil Performance Enhancement Using Micro Discreet Jets." AIAA Paper 2011-0941, 49th AIAA Aerospace Sciences Meeting, Orlando, FL, 4-7 January 2011.
- [9] A. Lefebvre, B. Dano, W. Bartow, M. Fronzo, and G. Zha, "Performance and energy expenditure of coflow jet airfoil with variation of mach number," *Journal of Aircraft*, vol. 53, no. 6, pp. 1757–1767, 2016.

- [10] A. Lefebvre and G. Zha, "Numerical simulation of pitching airfoil performance enhancement using co-flow jet flow control," *AIAA 31st Applied Aerodynamics Conference*, vol. 2517, 2013.
- [11] A. Lefebvre and G. Zha, "Co-flow jet airfoil trade study part i : Energy consumption and aerodynamic performance," *AIAA 32nd Applied Aerodynamics Conference*, vol. 2682, 2014.
- [12] A. Lefebvre and G. Zha, "Co-flow jet airfoil trade study part ii : Moment and drag," *AIAA 32nd Applied Aerodynamics Conference*, vol. 2683, 2014.
- [13] Yang, Yunchao and Zha, Gecheng, "Super-Lift Coefficient of Active Flow Control Airfoil: What is the Limit?," *AIAA Paper 2017-1693, AIAA SCITECH2017, 55th AIAA Aerospace Science Meeting, Grapevine, Texas*, p. 1693, 9-13 January 2017.
- [14] Lefebvre, A. and Dano, B. and Bartow, W. and Di Franzo, M. and Zha, G.-C., "Performance Enhancement and Energy Expenditure of Co-Flow Jet Airfoil with Variation of Mach Number." *AIAA Paper 2013-0490, AIAA Journal of Aircraft*, DOI: 10.2514/1.C033113, 2016.
- [15] Lefebvre, A. and Zha, G.-C., "Trade Study of 3D Co-Flow Jet Wing for Cruise Performance." *AIAA Paper 2016-0570, AIAA SCITECH2016, AIAA Aerospace Science Meeting, San Diego, CA, 4-8 January 2016*.
- [16] J. R. Burley II, L. S. Bangert, and J. R. Carlson, "Static investigation of circular-to-rectangular transition ducts for high-aspect-ratio nonaxisymmetric nozzles." *NASA Technical Paper 2534*, 1986.
- [17] P. R. Spalart and S. R. Allmaras, "A one-equation turbulence model for aerodynamic flows," in *30th Aerospace Sciences Meeting and Exhibit, Aerospace Sciences Meetings, Reno, NV, USA, AIAA Paper 92-0439*, 1992.
- [18] Shen, Y.Q., and Zha, G.C., "Large Eddy Simulation Using a New Set of Sixth Order Schemes for Compressible Viscous Terms," *Journal of Computational Physics*, vol. 229, pp. 8296–8312, doi:10.1016/j.jcp.2010.07.017, 2010.
- [19] Zha, G.C., Shen, Y.Q. and Wang, B.Y., "An improved low diffusion E-CUSP upwind scheme ," *Journal of Computer and Fluids*, vol. 48, pp. 214–220, Sep. 2011.
- [20] K. Xu and G.-C. Zha, "Design of high specific speed mixed flow micro-compressor for co-flow jet actuators." In *ASME Turbo Expo 2019 Turbomachinery Technical Conference and Exposition, Phoenix, Arizona, January 6-10, 2020*.
- [21] P. Patel and G.-C. Zha, "Investigation of mixed micro-compressor casing treatment using non-matching mesh interface." In *ASME Turbo Expo 2019 Turbomachinery Technical Conference and Exposition, Phoenix, Arizona, January 6-10, 2020*.
- [22] G.-C. Zha, Y.-C. Yang, Y. Ren, and B. McBreen, "Super-lift and thrusting airfoil of coflow jet-actuated by micro-compressors." *AIAA Paper 2017-3061, AIAA AVIATION 2018, Atlanta, GA, Submitted for publication in AIAA Journal* , 25 - 29 June 2018.
- [23] K. Xu, B. McBreen, Y. Ren, and G.-C. Zha, "Analysis of micro-compressor performance with integrated co-flow jet airfoil ducting system." *AIAA Paper 2017-3061, AIAA SciTech Forum, Orlando, FL, January 6-10, 2020*.
- [24] Y. Wang and G.-C. Zha, "Study of 3D Co-flow Jet Wing Induced Drag and Power Consumption at Cruise Conditions." *AIAA Paper 2019-0034, AIAA SciTech 2019, San Diego, CA, January 7-11, 2019*.

- [25] Y. Wang, Y.-C. Yang, and G.-C. Zha, “Study of Super-Lift Coefficient of Co-Flow Jet Airfoil and Its Power Consumption.” AIAA Paper 2019-3652, AIAA Aviation 2019, AIAA Applied Aerodynamics Conference, Dallas, Texas, 17-21 June 2019.
- [26] Y. Wang and G.-C. Zha, “Study of Mach Number Effect for 2D Co-Flow Jet Airfoil at Cruise Conditions.” AIAA Paper 2019-3169, AIAA Aviation 2019, AIAA Applied Aerodynamics Conference, Dallas, Texas, 17-21 June 2019.
- [27] Y. Ren and G.-C. Zha, “Design of Injection and Suction Ducts for Co-Flow Jet Airfoils with Embedded Micro-Compressors Actuator.” AIAA Aviation Forum, 2018 Flow Control Conference, Atlanta, Georgia, 25-29 June 2018.
- [28] Y.-Q. Shen and G.-Z. Zha, “Generalized finite compact difference scheme for shock/complex flowfield interaction,” *Journal of Computational Physics*, vol. doi:10.1016/j.jcp.2011.01.039, 2011.
- [29] Shen, Y.Q., Zha, G.C., and Wang, B.Y., “Improvement of Stability and Accuracy of Implicit WENO Scheme,” *AIAA Journal*, vol. 47, pp. 331–334, DOI:10.2514/1.37697, 2009.
- [30] Shen, Y.Q., Zha, G.C., and Chen, X., “High Order Conservative Differencing for Viscous Terms and the Application to Vortex-Induced Vibration Flows,” *Journal of Computational Physics*, vol. 228(2), pp. 8283–8300, doi:10.1016/j.jcp.2009.08.004, 2009.
- [31] Shen, Y.Q., and Zha, G.C., “Improvement of the WENO Scheme Smoothness Estimator,” *International Journal for Numerical Methods in Fluids*, vol. 64., pp. 653–675, DOI:10.1002/fld.2186, 2009.
- [32] Zha, G.C., and Bilgen, E., “Numerical Solutions of Euler Equations by Using a New Flux Vector Splitting Scheme,” *International Journal for Numerical Methods in Fluids*, vol. 17, pp. 115–144., 1993.
- [33] Zha, G.C., and Bilgen, E., “Numerical Study of Three-Dimensional Transonic Flows Using Unfactored Upwind Relaxation Sweeping Algorithm,” *Journal of Computational Physics*, vol. 125, pp. 425–433., 1996.
- [34] Wang, B.Y., Hu, Z. and Zha, G.C., “A General Sub-Domain Boundary Mapping Procedure For Structured Grid CFD Parallel Computation,” *AIAA Journal of Aerospace Computing, Information, and Communication*, vol. 5, pp. 425–447, 2008.
- [35] Y.-Q. Shen, G.-C. Zha, and B.-Y. Wang, “Improvement of Stability and Accuracy of Implicit WENO Scheme,” *AIAA Journal*, vol. 47, pp. 331–344, 2009.
- [36] Y. Wang and G.-C. Zha, “Study of Mach Number Effect for 3D Co-Flow Jet Wings at Cruise Conditions.” AIAA Paper 2020-0045, AIAA SciTech 2020, AIAA SciTech 2020 Forum, Orlando, Florida, 6-10 January 2020.